Acta Materialia 98 (2015) 288–296

Contents lists available at ScienceDirect

Acta Materialia

journal homepage: www.elsevier.com/locate/actamat

Phase stability of non-equiatomic CoCrFeMnNi high entropy alloys

Duancheng Ma [a,*], Mengji Yao [a], K.G. Pradeep [a,b], Cemal C. Tasan [a], Hauke Springer [a], Dierk Raabe [a]

[a] Max-Planck-Institut für Eisenforschung GmbH, Max-Planck-Straße 1, 40237 Düsseldorf, Germany
[b] Materials Chemistry, RWTH Aachen University, Kopernikusstraße 10, 52074 Aachen, Germany

ARTICLE INFO

Article history:
Received 21 May 2015
Accepted 13 July 2015

Keywords:
High entropy alloy
Phase stability
Thermodynamics
CALPHAD

ABSTRACT

The objective of this study is to experimentally and theoretically investigate the phase stability of non-equiatomic $Fe_xMn_{62-x}Ni_{30}Co_6Cr_2$ based high entropy alloys, where x ranges from 22 to 42 at.%. Another aim is to systematically and critically assess the predictive capability of the CALPHAD approach for such high entropy alloy systems. We find that the CALPHAD simulations provide a very consistent assessment of phase stability yielding good agreement with experimental observations. These include the equilibrium phase formation at high temperatures, the constituent phases after non-equilibrium solidification processes, unfavorable segregation profiles inherited from solidification together with the associated nucleation and growth of low temperature phases, and undesired martensitic transformation effects. Encouraged by these consistent theoretical and experimental results, we extend our simulations to other alloy systems with equiatomic compositions reported in the literature. Using these other equiatomic model systems we demonstrate how systematic CALPHAD simulations can improve and accelerate the design of multicomponent alloy systems.

1. Introduction

High entropy alloys (HEA) are multicomponent (5 or more) massive solid solutions with an equiatomic or a near equiatomic composition [1–6]. The original ideal of investigating multicomponent alloys in equal or near-equal proportions represents a new alloy exploration strategy [7–10,6]. Instead of starting from a corner of a phase diagram with one prevalent base element, it has been suggested that new materials could be identified by directly producing equiatomic compositions with multiple components. The term "high entropy alloys" was introduced by Yeh et al. [2], based on the hypothesis that the high configurational entropy would stabilize the solid solution phase over competing intermetallic and elemental phases [11]. A well-studied HEA is the Cantor alloy *i.e.* $Co_{20}Cr_{20}Fe_{20}Mn_{20}Ni_{20}$ (at.%) which develops a single phase fcc solid solution *e.g.* [9,12–16]. Recently, it has been shown that a non-equiatomic composition of this alloy system also exhibits a single phase fcc solid solution irrespective of its slightly lower mixing entropy [17,18].

The objective of this study is two-fold. One focus is the prediction and analysis of the phase stability of this alloy system *i.e.* $Fe_xMn_{62-x}Ni_{30}Co_6Cr_2$ (at.%, x = 22, 27, 32, 37, and 42), while varying the Fe and Mn contents, and maintaining the compositions of Cr, Co and Ni constant. The configurational entropy of these alloys ranges from 1.295 to 1.334 k_B/atom (k_B is the Boltzmann constant) which yields 80–83% of that in equiatomic composition (1.6094 k_B/atom) as shown in Fig. 1.

Another focus is to explore the feasibility of using the CALPHAD (CALculation of PHAse Diagrams) method for future knowledge based approaches to the design of HEAs. Compared with other approaches for designing HEAs (*e.g.* empirical rules [19–26], or ab initio based methods [27,28]), the CALPHAD method provides an optimal balance between efficiency and accuracy. On the other hand, most multicomponent systems are not fully covered by the available CALPHAD databases. Instead, current CALPHAD simulations of multicomponent systems are based on the extrapolation from binary, ternary, and, (perhaps) quaternary systems [29]. Hence, the accuracy of the corresponding predictions yielded by using a CALPHAD approach needs to be critically evaluated.

This paper is organized as the follows: The synthesis, heat treatment and methods of phase identification are described in Section 2. The employed CALPHAD method will be briefly introduced in Section 3. The experimental results will be presented in Section 4.1. In Section 4.2 we show the calculated phase diagram, as well as corresponding CALPHAD simulations to predict the phases and compositions resulting from solidification and annealing followed by water quenching. We then compare and discuss the experimental and theoretical results in Section 5. In Section 6, we further examine the predictive capacities of

* Corresponding author.
E-mail address: d.ma@mpie.de (D. Ma).

http://dx.doi.org/10.1016/j.actamat.2015.07.030
1359-6454/

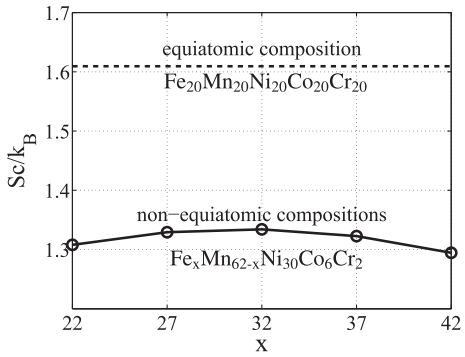

Fig. 1. The configurational entropy (S_c) of the non-equiatomic compositional HEAs ($Fe_xMn_{62-x}Ni_{30}Co_6Cr_2$) as a function of x (atomic fraction of Fe). The horizontal dashed line is the S_c of the HEA at the equiatomic composition ($Fe_{20}Mn_{20}Ni_{20}Co_{20}Cr_{20}$). S_c is in k_B (Boltzmann constant) per atom.

CALPHAD by comparing the corresponding simulation results with observations presented in the experimental study by Otto et al. [12]. Finally, we summarize this study in 7.

2. Experiments: alloy preparation and phase identification

2.1. Alloy preparation: synthesis and heat treatment

The conventional approach for investigating the microstructure and mechanical properties of novel metallic structural materials typically consists of iterative experimental loops including synthesis of a single charge, hot and/or cold deformation, heat treatment, machining of tensile specimens and mechanical testing. Specifically, when the alloy system of interest has not been completely understood, *e.g.* in terms of thermodynamic stability and corresponding process parameters, this conventional approach is often too time-consuming for efficient investigations and rapid maturation of complex alloy systems. The here undertaken research into the chemistry dependency of the phase stability of non-equiatomic high entropy alloys is thus a good example where the deployment of a novel high-throughput bulk metallurgical synthesis and processing procedure, termed rapid alloy prototyping (RAP), can lead to a greatly increased efficiency in the alloy design process [30].

Five compositions of HEAs, *i.e.* $Fe_xMn_{62-x}Ni_{30}Co_6Cr_2$ (at.%, x = 22, 27, 32, 37, and 42), were produced following the RAP approach, which is schematically illustrated in Fig. 2 and presented in greater detail in [30]. Starting from metals with a purity higher than 99.9 wt.%, melting and casting was performed in a vacuum induction furnace under an Ar atmosphere of 400 mbar. After casting the first melt with 20 at.% Mn into Cu-moulds standing on a water-cooled Cu-plate, pre-calculated amounts of Mn were added to the remaining melt and the next mould was positioned under the crucible. The nominal and the actual chemical compositions of the so obtained five alloys are listed in Table 1. The average cooling rate during solidification was measured to be of the order of $10\,K \cdot min^{-1}$. The cast rectangular blocks of $10 \times 50 \times 130\,mm^3$ were subsequently hot-rolled at 1123 K to 5 to 10 mm thickness at air. Homogenization was performed by annealing the as-rolled sheets at 1473 K for 2 h under Ar atmosphere followed by water quenching.

2.2. Constituent phase identification

DSC (differential scanning calorimetry) was conducted on as-cast alloys, starting from ~300 K (room temperature) to 1573 K in Ar atmosphere. DSC experiments were carried out in a SETARAM Setsys 16/18 device using heating rates of 5 and 10 K/min.

EBSD (electron back scattered diffraction) measurements were conducted on the samples which were annealed (1473 K for 2 h) followed by water quenching. A 6490 JEOl tungsten filament-SEM equipped with a TSL OIM EBSD system was used, operating at 15 kV.

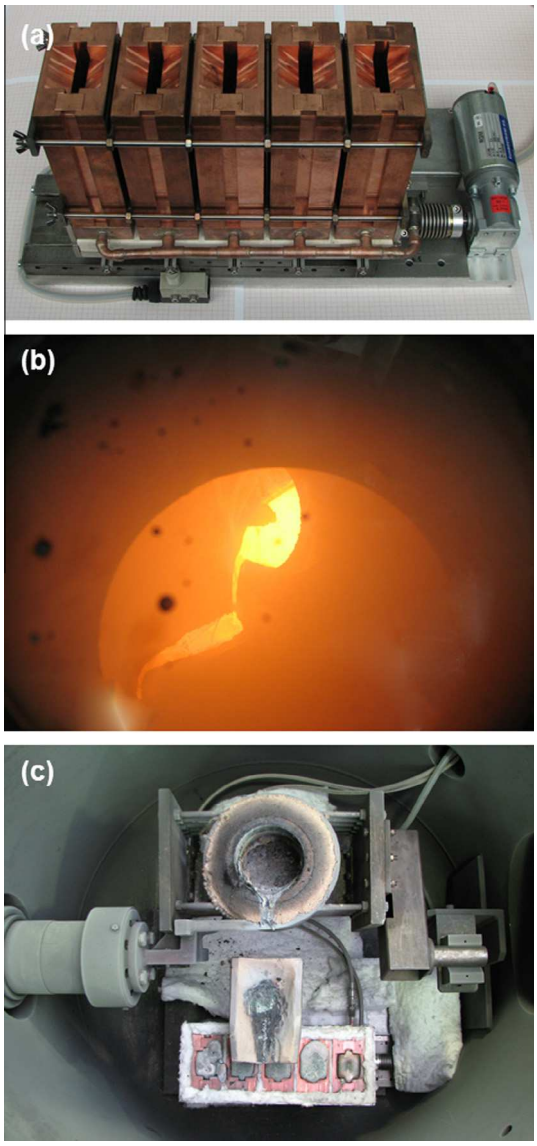

Fig. 2. Illustrations of the high-throughput synthesis procedure applied here: (a) Cu-moulds placed on a linear stage for casting 5 different alloys from one melting operation, (b) view of a combinatorial casting, (c) opened furnace after completing synthesis.

Table 1
The chemical compositions of the synthesized HEAs.

Nominal composition/at.%	Actual composition/at.%
$Fe_{22}Mn_{40}Ni_{30}Co_6Cr_2$	$Fe_{25.7}Mn_{37.6}Ni_{28.5}Co_{5.8}Cr_{2.4}$
$Fe_{27}Mn_{35}Ni_{30}Co_6Cr_2$	$Fe_{29.4}Mn_{33.9}Ni_{28.5}Co_{5.8}Cr_{2.4}$
$Fe_{32}Mn_{30}Ni_{30}Co_6Cr_2$	$Fe_{40.0}Mn_{27.0}Ni_{25.7}Co_{5.2}Cr_{2.1}$
$Fe_{37}Mn_{25}Ni_{30}Co_6Cr_2$	$Fe_{41.1}Mn_{24.1}Ni_{27.1}Co_{5.5}Cr_{2.2}$
$Fe_{42}Mn_{20}Ni_{30}Co_6Cr_2$	$Fe_{42.2}Mn_{20.7}Ni_{28.9}Co_{5.9}Cr_{2.3}$

3. CALPHAD simulations

The CALPHAD (CALculation of PHAse Diagrams) simulations were performed on the platform of Thermo-Calc [31] using the database TCFE7 (Fe-alloys database version 7).

Phase diagrams calculated by CALPHAD are by definition equilibrium phase diagrams, while most corresponding experiments represent materials that are often far away from their equilibrium state.

In order to resolve this problem two other types of CALPHAD-based simulations were performed besides the prediction of the actual equilibrium phase diagrams: (1) simulation of the non-equilibrium solidification process by using the Scheil model. This model was designed to predict segregation profiles that are created during solidification. The Scheil model considers kinetic effects for predicting chemical gradients that form during solidification of metallurgical alloys. It is based on assuming three boundary conditions that are characteristic for solidification of alloys: (a) diffusion inside the liquid is assumed to be infinite; (b) diffusion in the solid is assumed to be zero; (c) equilibrium at the liquid–solid interface is maintained. (2) comparison of the Gibbs free energies of the bcc and fcc solid solutions for the specific compositions of $Fe_xMn_{62-x}Ni_{30}Co_6Cr_2$, in a temperature range between 0 and 1500 K. These two additional types of simulations correspond to the situations found in the as-cast and in the annealed plus water quenched states, respectively.

It should be mentioned that the interdiffusion in $Fe_{20}Mn_{20}Ni_{20}Co_{20}Cr_{20}$ (at.%) was found to be slower than that conventional more dilute face-centered cubic alloys [32], such as austenitic stainless steels. This is an indication that the self-diffusion in $Fe_{20}Mn_{20}Ni_{20}Co_{20}Cr_{20}$ (at.%) is slower, which may most likely apply also to the alloy compositions probed in this study. Hence, the second boundary condition assumption that we used in the Scheil model, namely, that the diffusion in the solid state is zero, is reasonable for the alloy system analyzed in this study.

4. Results

4.1. Results of DSC and EBSD characterization

For the as-cast alloys, the DSC traces presented in Fig. 3 show no endothermic or exothermic peaks for all alloys, indicating that no solid state phase transformation has taken place between room temperature and melting. It can be noted that with an increase in the Fe concentration, the melting point also increases.

Below 600 K, there are fluctuations on the DSC curves, which are more pronounced for the larger heating rate of 10 K/min. This is due to the fact that for a given heating rate, a certain time is needed in the initiation stage to reach a stable heat flux.

Fig. 4 shows the EBSD phase maps of $Fe_xMn_{62-x}Ni_{30}Co_6Cr_2$ HEAs. Only fcc phase was detected in all investigated alloys which were homogenized at 1473 K for 2 h followed by water quenching.

4.2. Results of the CALPHAD calculation

4.2.1. Equilibrium phase diagram

The stable phase diagram is calculated by including all possible phases that are listed in the database TCFE7 into the CALPHAD prediction. The calculated isopleth of the phase diagram is shown in Fig. 5, *i.e.* $Fe_xMn_{62-x}Ni_{30}Co_6Cr_2$, and x (Fe at.%) ranges from 20 to 45.

According to the isopleth shown in Fig. 5, after solidification, the equilibrium solidified phase is a γ(fcc) solid solution. As the temperature drops, γ(fcc) decomposes into γ(fcc) + α(bcc) solid solution phases. At 600 K in this two-phase region, the volume fraction of α(bcc) is around 20% as shown in the left hand side of Fig. 6. When the temperature further drops, σ phase appears in addition to γ(fcc) and α(bcc). At 300 K (around room temperature) in the three-phase region, the volume fraction of α(bcc) increases compared with that at 600 K, and a small amount of σ phase with about 3% volume fraction appears (see the right hand side of Fig. 6).

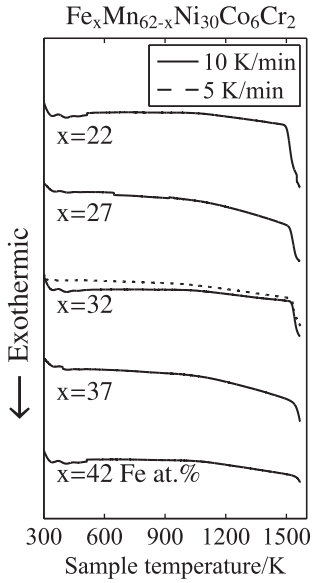

Fig. 3. DSC measurements of the $Fe_xMn_{62-x}Ni_{30}Co_6Cr_2$ alloy, heating from room temperature up to the melting point. No solid state phase transformation is detected between room temperature and the respective melting points. The solid line indicates a heating rate of 10 K/min and the dashed line of 5 K/min. The data show fluctuations at low temperatures. This is due to the fact that for a given heating rate, a sufficient time is needed to reach a state of stable heat flux.

Fig. 7 shows the atomic concentrations of the γ(fcc) and α(bcc) phases at 600 K, and also of the γ(fcc), α(bcc), and σ at 300 K. The α(bcc) phase is basically a Fe-Co solid solution with a large amount of Fe, *i.e.* ~70–90 at.%. It also contains a very small amount (<1 at.%) of Mn, Ni, and Cr at 600 K, and a negligible amount of the same elements at 300 K. In the σ phase, there are only three major elements, *i.e.* Fe, Mn, and Cr. In γ(fcc), the major elements are Fe, Mn, and Ni. The concentration of Fe in γ(fcc) is below those of Mn and Ni, and as the temperature drops, the content of Fe that is solved in the γ(fcc) phase also decreases. The concentrations of Mn and Ni are nearly identical in γ(fcc).

It has to be noted that in Fig. 5, when the Fe content increases, the liquidus and solidus lines of $Fe_xMn_{62-x}Ni_{30}Co_6Cr_2$ also increase. This is consistent with the observation in the DSC measurement shown in Fig. 3 that the melting point increases with the Fe content.

4.2.2. Non-equilibrium solidification (Scheil model)

According to the Scheil simulations, the solid phase obtained after a non-equilibrium solidification process is always γ(fcc) for all compositions, which is consistent with the XRD measurements [33].

Fig. 8 shows the changing elemental compositions in the solid γ(fcc) phase during solidification. Here, we only show two alloy compositions, *i.e.* $Fe_{22}Mn_{40}Ni_{30}Co_6Cr_2$ and $Fe_{42}Mn_{20}Ni_{30}Co_6Cr_2$ as representative examples. In each subfigure of Fig. 8, the compositions predicted at the highest temperature correspond to the compositions in the center of the dendrite. The final compositions predicted for the lowest temperatures correspond to the compositions in the center of the interdendritic regions. Fig. 8 shows that the most pronounced segregation occurs for the elements Fe, Ni, and Mn. Fe segregates to the dendrites, while Mn and Ni segregate to the interdendritic regions. Cr and Co only slightly segregate

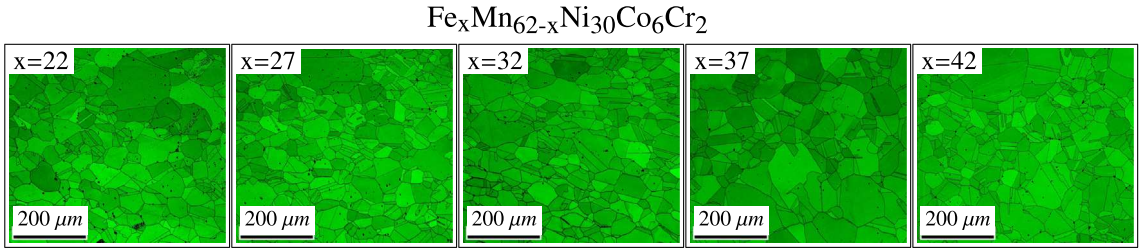

Fig. 4. Phase and image quality (IQ) maps of $Fe_xMn_{62-x}Ni_{30}Co_6Cr_2$ (x = 22, 27, 32, 37, 42) measured by using EBSD. Only fcc (green color) is detected. (For interpretation of the references to color in this figure legend, the reader is referred to the web version of this article.)

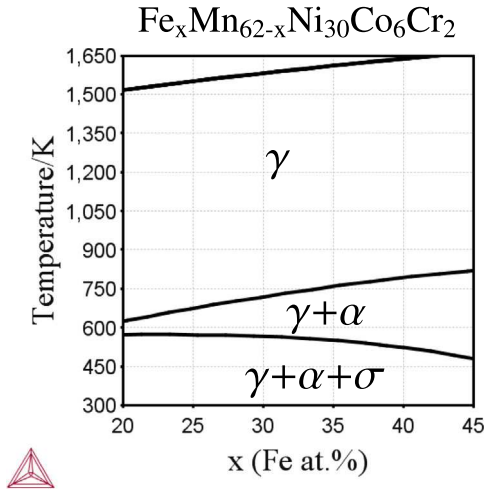

Fig. 5. Phase diagram calculated by CALPHAD method on the platform of Thermo-Calc [31], taking all possible phases in the database (TCFE7) into account.

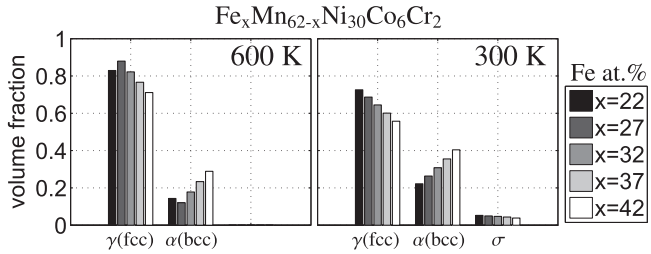

Fig. 6. Volume fractions of the γ(fcc), α(bcc), and σ phases at (left) 600 K and (right) 300 K determined by CALPHAD for the global alloy compositions of $Fe_xMn_{62-x}Ni_{30}Co_6Cr_2$ (x = 22, 27, 32, 37, and 42).

during gradual cooling, hence, causing practically no elemental gradients across the dendrites.

The segregation trend predicted by the non-equilibrium solidification simulation is consistent with the experimental observations made on the as-cast CrCoFeMnNi alloy in equiatomic composition by Laurent-Brocq et al. [34]. They found that Fe, Cr, Co segregate into the dendrite, while Mn and Ni segregate to the interdendritic regions.

4.2.3. Phase stability between fcc and bcc solid solution at identical chemical composition

The Gibbs free energies of the γ(fcc) phase after subtracted by the corresponding Gibbs free energies of the α(bcc) phase as a function of temperature are shown in Fig. 9. Note that γ(fcc) and α(bcc) have the same composition in this case. The data show that within the temperature range between 0 and 1500 K, γ(fcc) is always stable over α(bcc). This indicates that a martensitic transformation from γ(fcc) to α(fcc) by quenching from elevated temperatures is thermodynamically not favorable.

There is a critical temperature above which the stability of the γ(fcc) phase decreases as the temperature rises, below which it increases as the temperature increases. This critical temperature increases as the Fe content increases. This indicates that the stability of γ(fcc) decreases as the Fe content increases, which is consistent with the predicted phase diagram shown in Fig. 5, indicating that the transition temperature from the single phase region (γ(fcc)) into the two-phase region (γ(fcc) + α(bcc)) becomes higher as the Fe content increases.

5. Comparison between experiments and CALPHAD simulations

For HEAs with their intrinsically slow diffusion kinetics, 3 possible scenarios are conceivable to occur during cooling after solidification: (1) the high temperature phase is retained; (2) due to segregation during non-equilibrium solidification, the local chemical composition can be close to the chemical compositions of the low temperature phases. In case that long distance diffusion is not required – which is actually a characteristic feature of HEAs owing to their intense mixing state – at low temperatures phase separation can occur; (3) occurrence of a martensitic transformation.

In the experiments, only a fcc solid solution was detected at room temperature, although CALPHAD had predicted the occurrence of three phases at room temperature, *i.e.* γ(fcc), α(bcc), and σ (see Fig. 5). Thus, the observed single fcc solid solution phase in the investigated HEAs at room temperature is probably the retained quenched-in high temperature phase, similar to other HEAs exhibiting a single solid solution phase, as suggested by Zhang et al. [36] and Pradeep et al. [37].

Despite the fact that the first scenario is consistent with the experimental observations, the CALPHAD simulations can also help to exclude the latter two scenarios. When comparing the compositions of the low temperature phases, *i.e.* α(bcc) and σ as shown in Fig. 7 in conjunction with the segregation trends revealed by the Scheil model in Fig. 8, the second possible scenario can also be excluded. For instance, the concentrations of Ni in both, the α(bcc) and the σ phases are nearly negligible (see Fig. 7). Ni, however, is not depleted in either the dendritic or interdendritic regions (see Fig. 8). Hence, this type of segregation is not in favor of the nucleation and growth of α(bcc) and σ phase at low temperatures.

The third scenario of a martensitic transformation from γ(fcc) to α(bcc) can also be excluded: Fig. 9 shows that the Gibbs free energy of γ(fcc) is always lower than that of the α(bcc) phase between 0 and 1500 K for all the compositions $Fe_xMn_{62-x}Ni_{30}Co_6Cr_2$ with x ranging between 22 and 42.

Thus, although CALPHAD predictions are typically used for equilibrium phase diagram calculations the approach we present here enables us to also convey partitioning and corresponding

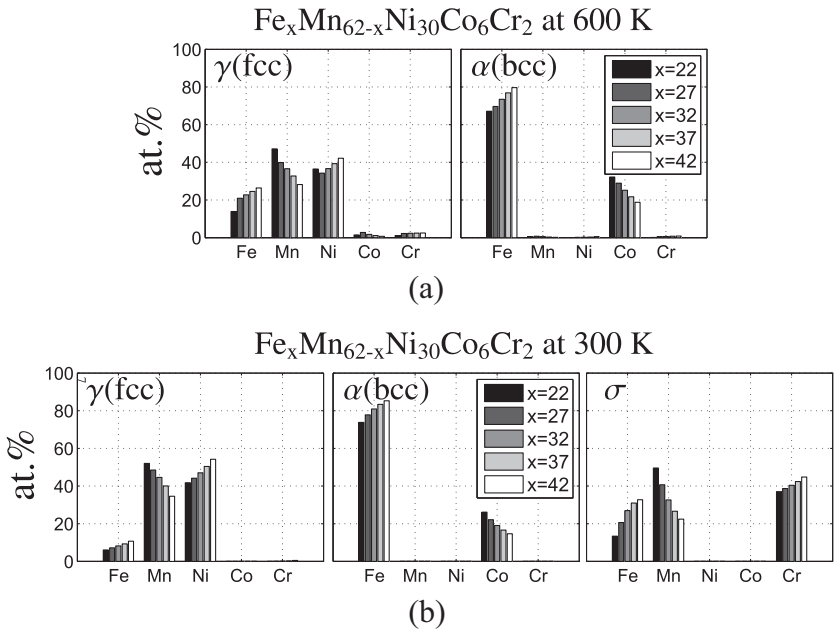

Fig. 7. The concentrations (at.%) of Fe, Mn, Ni, Co, and Cr in (a) γ(fcc) and α(bcc) at 600 K; (b) γ(fcc), α(bcc), and σ at 300 K.

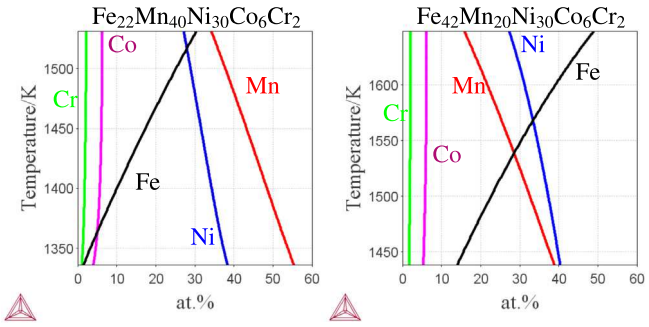

Fig. 8. The atomic concentrations of Fe (black), Mn (red), Ni (blue), Co (magenta), and Cr (green) in the solid phase (γ(fcc)) at the liquid–solid interface during solidification determined by the Scheil model as implemented in the Thermo-Calc modeling approach for the nominal compositions of (left) $Fe_{22}Mn_{40}Ni_{30}Co_6Cr_2$ and (right) $Fe_{42}Mn_{20}Ni_{30}Co_6Cr_2$. The compositions at the highest temperature correspond to the compositions in the center of the dendrite and those at the lowest temperature correspond to the compositions at the center of the interdendritic region. (For interpretation of the references to color in this figure legend, the reader is referred to the web version of this article.)

Scheil–type segregation predictions which present altogether excellent tools for identifying suitable compositional and cooling rate regimes when aiming at targeting equilibrium or non-equilibrium HEAs.

A further important aspect to be considered is that owing to the very sluggish diffusion kinetics characteristic of HEAs it seems plausible that the few true solid solution single phase alloys that have been identified so far are most likely kinetically stabilized and would thermodynamically probably tend to decompose after sufficiently long diffusion times.

6. Revisiting HEAs in equiatomic composition

In Sections 4.1, 4.2, 5, we revealed that for the here investigated HEAs, CALPHAD provides very consistent results when compared to experiments. By considering both the relevant enthalpy and entropy contributions, the CALPHAD models should ideally be able to predict the phase formation in other HEA systems. Hence, in order to test the versatility and suitability of using such models in predicting the solid solution forming HEA compositions, we verify the claim by performing CALPHAD simulations for other reported

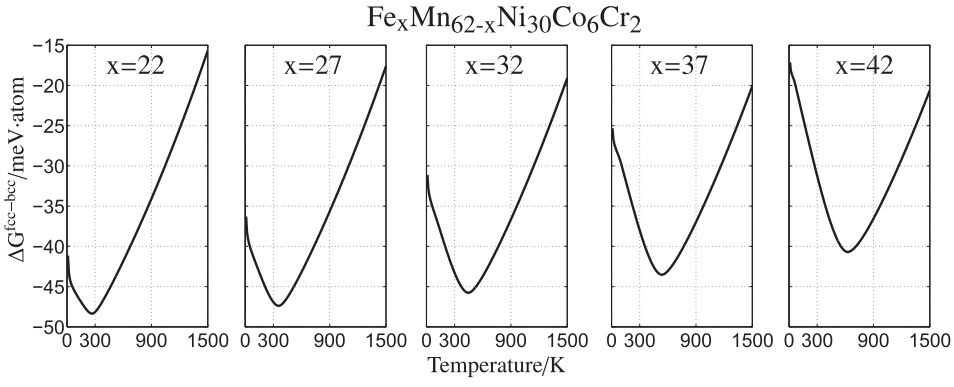

Fig. 9. Gibbs free energy difference obtained by subtracting that of the γ(fcc) phase by the α(bcc) ($\Delta G^{fcc-bcc}$) at the composition of $Fe_xMn_{62-x}Ni_{30}Co_6Cr_2$ between 0 and 1200 K.

compositions. Moreover, the CALPHAD method is computationally more efficient compared to ab initio based methods [27,28].

In this section, we thus compare the results of CALPHAD simulations with experimental observations that were published on six different 5-component alloys in equiatomic composition by Otto et al. [12]. In [12], the CALPHAD simulations were conducted on the associated binary systems, while in this study the CALPHAD simulation are directly conducted on the 5-component systems. In what follows, we skip the atomic concentration units in the chemical formula, *e.g.* we use CoCrFeMnNi instead of $Co_{20}Cr_{20}Fe_{20}Mn_{20}Ni_{20}$, because they are all of equiatomic composition.

6.1. Comparison between CALPHAD simulations and experiments reported by Otto et al. [12]

In Table 2 the constituent phases predicted by CALPHAD are compared with the experimental observations presented in [12].

CoCrFeMnNi By using CALPHAD, both the equilibrium phase at 1273 K and the non-equilibrium solidified phase assume fcc crystal structure for the prototype Cantor HEA CoCrFeMnNi. This result is consistent with the experimental observations when assuming, as discussed in the preceding section, *i.e.* that the fcc phase that is first formed upon solidification at a temperature of 1273 K, is also retained at room temperature due to kinetic constraints.

The corresponding non-equilibrium solidification simulation reveals the same trend as the observation by Laurent-Brocq et al. [34] *i.e.* that Fe, Cr, and Co segregate to the dendrite core, and Mn and Ni segregate to the interdendritic regions. The partition coefficient[1] was estimated to be 0.74 [34], which is similar to the one estimated by CALPHAD, *i.e.* 0.875.

CoCrFeMn*Cu* For CoCrFeMn*Cu*, in the experiments, two fcc solid solutions were observed, *i.e.* Cu is depleted in fcc^{exp1} (Cu at.% < 4) and is enriched in fcc^{exp2} (Cu at.% = 74) (see Table 3). The main solidified constituent phases predicted by the Scheil model is fcc^{s} with 92% volume fraction. Cu is enriched in the interdendritic regions of fcc^{s}, which is consistent with the microstructural observation in [12] *i.e.* fcc^{exp2} was found in regions resembling the interdendritic zone. A similar observation of Cu depletion and enrichment, due to sequential partitioning, was also made in AlCrCuFeNiZn [37].

Yet, a discrepancy remains between the CALPHAD simulations and the experiment, *i.e.* a small amount of σ phase was detected in the CoCrFeMn*Cu* experiment, but neither the equilibrium simulation nor the Scheil model predicts the formation of the σ phase. In [12], the formation of σ is interpreted as a result of depletion/absence of the fcc stabilizing elements Mn and Ni. According to the equilibrium simulation and the predictions obtained by the Scheil model, the Mn content is not depleted in either the fcc or the bcc phase.

The equilibrium phases were also predicted on another CALPHAD platform in Ref. [36]. Accordingly, at 1123 K, the same constituent phases, *i.e.* fcc + fcc + bcc were also predicted. In the Cu enriched fcc phase, the concentrations of Cu and Mn are 88 and 9 at.%, respectively, while in the Cu depleted fcc phase, the Cu concentration is 4.8 at.%. The general trend of the constituent phases and their respective compositions predicted in this study and in [36] are in general consistent with each other.

The discrepancy *i.e.* the presence of the σ phase in the experiment and the absence of it in the theoretical prediction, is attributed to the fact that the experimentally observed phases are in a transient state between the as-cast state and the equilibrium state.

***Ti*CrFeMnNi** According to the predictions of the Scheil model (see Table 2), *Ti*CrFeMnNi starts to solidify at ~1526 K, reaching a complete solid state at ~678 K, which significantly deviates from the reported melting temperature, *i.e.* the melting point of this alloy clearly lies above observed 1237 K [12]. Hence, it needs to be stated that CALPHAD simulation for *Ti*CrFeMnNi is not reliable. The origin of the error could be (i) the quality of the underlying thermodynamic approximations, specifically regarding the influence of Ti as a solid solution element, is quantitatively not adequate; (ii) the assumptions used regarding partitioning and kinetic transients in the Scheil model are not sufficiently realistic for this system.

Co*Mo*FeMnNi The predicted equilibrium phases occurring in the system Co*Mo*FeMnNi at 1237 K are fcc^{eq} and μ^{eq} (Table 2). This prediction is consistent with the experimental observations. The compositions of fcc^{eq} and μ^{eq} are also very close to the measurements (see Table 3). The volume fraction of μ^{eq} is predicted to be 31%, which is also in agreement with observations as the experiments reveal large fractions of μ^{exp} phases. Thus, this result suggests that the heat treatment conducted by Otto et al. [12] *i.e.* annealing at 1237 K for 3 days, is sufficient for Co*Mo*FeMnNi to reach its equilibrium state.

Co*V*FeMnNi It is interesting to observe that the predicted phase for the system Co*V*FeMnNi is single solid solution *i.e.* fcc^{eq} at 1237 K (see Table 2). Among the HEAs studied in [12], the microstructure of the alloy Co*V*FeMnNi is the only one which is close to that of CoCrFeMnNi, except that in Co*V*FeMnNi, a small amount of σ phase was observed. The solidified phases as predicted by the Scheil model are fcc^{s} with 92% volume fraction and a small portion of bcc^{s}. V is to some extent enriched in the bcc^{s} phase. In the experiment, V is also slightly enriched in the σ phase. We speculate that the experimentally observed σ phase might precipitate by consuming the bcc^{s} phase, because the composition of the bcc^{s} phase promotes the formation of the experimentally observed σ phase. In addition to the chemical composition, according to the Scheil model, bcc^{s} forms during cooling subsequent to fcc^{s}, *i.e.* bcc^{s} might be a phase to be observed in interdendritic regions. Indeed in the experiment, the σ^{exp} phase was also observed in the interdendritic/integranular regions. The experimentally observed phases are probably at the intermediate state between the as-cast state and the equilibrium state, similar as observed for the system CoCrFeMn*Cu*.

CoCr*V*MnNi As for the CoCr*V*MnNi alloy, both the equilibrium calculation at 1237 K and the Scheil model predicts a mixture of fcc and bcc phases, while a mixture of fcc and σ was observed in the experiments. V is slightly enriched in the solidified bcc^{s} phase according to Scheil model, but the enrichment is not as high as that in Co*V*FeMnNi. The only consistency which can be found between CALPHAD and the experiment for this system is that in the experiments a fcc^{exp} phase is found in the interdendritic regions, while the Scheil model predicts fcc^{s} to appear after the bcc^{s} phase during solidification.

6.2. Discussion of the comparison between CALPHAD simulations and experiments reported by Otto et al. [12]

According to the thermodynamic analysis provided above, these six different alloy systems can be grouped into three categories: (1) those where the equilibrium state predicted by CALPHAD simulation is in agreement with experiment, such as found for CoCrFeMnNi and Co*Mo*FeMnNi; (2) those where the experimentally observed phases seem to be in a transient state between the as-cast state and the equilibrium state, such as observed for CoCrFeMn*Cu* and CoCr*V*MnNi; (3) those where the CALPHAD

[1] The partition coefficient is defined as the ratio of the concentration of solutes in the solid over the concentration of solutes in the liquid. In [34], the partition coefficient is approximated by the ratio of the solute concentration in the first formed dendrites over the nominal solute concentration. As for the case of CoCrFeMnNi, a semi-binary system is assumed, which is (CoCrFe)–(MnNi) in which (MnNi) is considered to act as the solute couple.

Table 2
Comparison of constituent phases in equiatomic compositional HEAs predicted by CALPHAD and observed in experiments [12]. In the experiments, the cast ingots were annealed for 3 days in evaculated quartz capsules at 1273 K, except for CoCrFeMn*Cu* which was annealed at 1123 K [12]. Accordingly, in the CALPHAD simulations, the equilibrium constituent phases are calculated at 1273 K, except for CoCrFeMn*Cu* at 1123 K. The Scheil model is applied to obtain the constituent phases in the solid during the non-equilibrium solidification process. As for *Ti*CrFeMnNi, besides χ and Laves, there were two other phases which were observed, but not identified in [12]. The superscript eq means that the phase is predicted assuming equilibrium state; the superscript s means that the phase is predicted assuming non-equilibrium solidification; the superscript exp means that the phase is observed and reported in [12].

	CALPHAD (this study)		Experiments [12]
CoCrFeMnNi	at 1273 K	fcc^{eq}	fcc^{exp}
	Scheil	fcc^{s}	
CoCrFeMn*Cu*	at 1123 K	fcc^{eq1}+fcc^{eq2}+bcc^{eq}	fcc^{exp1}+fcc^{exp2}+σ^{exp}
	Scheil	fcc^{s}+bcc^{s}	
Co*Mo*FeMnNi	at 1273 K	fcc^{eq}+μ^{eq}	fcc^{exp}+μ^{9m}
	Scheil	σ^{s}+fcc^{s}	
*Ti*CrFeMnNi	at 1273 K	fcc^{eq}+$Laves^{eq}$+bcc^{eq}	χ^{exp}+$Laves^{exp}$+2 other phases
	Scheil*	bcc^{s}+$Laves^{s}$+fcc^{s}+Ni_3Ti^{s}+σ^{s}+$NiTi^{s}$	
Co*V*FeMnNi	at 1273 K	fcc^{eq}	fcc^{exp}+σ^{exp}
	Scheil	fcc^{s}+bcc^{s}	
CoCr*V*MnNi	at 1273 K	fcc^{eq}+bcc^{eq}	fcc^{exp}+σ^{exp}
	Scheil	bcc^{s}+fcc^{s}	

* The non-equilibrium solidification process of *Ti*CrFeMnNi predicted by the Scheil model starts at ~1526 K and ends at ~678 K. In the experiments, however, the melting point is higher than 1273 K.

Table 3
Comparison of compositions of the constituent phases in equiatomic compositional HEAs predicted by CALPHAD and measured in experiments [12]. In the experiments, the cased ingots were annealed for 3 days in evaculated quartz capsules at 1273 K, except for CoCrFeMn*Cu* which was annealed at 1123 K [12]. Accordingly, in the CALPHAD simulations, the constituent phases are calculated at 1273 K, except for CoCrFeMn*Cu* at 1123 K. The Scheil model is applied to obtain the compositions of the constituent phases in the solid during solidification. The superscript eq means that the phase is predicted assuming equilibrium state; the superscript s means that the phase is predicted assuming non-equilibrium solidification; the superscript exp means that the phase is observed and reported in [12]. For the phases after the non-equilibrium solidification process, two compositions are gives, one of which is for the dendrite core (D), and another one which applies to the interdendritic region (I). V% is the volume fraction. N/A: not available.

	CALPHAD (this study) at.%							Experiments [12] at.%					
CoCrFeMn*Cu*		Co	Cr	Fe	Mn	*Cu*	V%		Co	Cr	Fe	Mn	*Cu*
	fcc^{eq1}	24	15	26	22	13	49						
	fcc^{eq2}	19	2	9	21	49	28						
	bcc^{eq}	12	52	21	15	~0	23	fcc^{exp1}	N/A	N/A	N/A	N/A	<4
	fcc^{s} D	20	18	27	20	15	92	fcc^{exp2}	<3	<3	<3	19	74
	I	15	4	1	19	61		σ^{exp}	N/A	N/A	N/A	N/A	N/A
	bcc^{s} D	13	51	21	14	1	8						
	I	9	76	2	13	0							
Co*Mo*FeMnNi		Co	*Mo*	Fe	Mn	Ni	V%		Co	*Mo*	Fe	Mn	Ni
	fcc^{eq}	20	9	20	25	26	69						
	μ^{eq}	20	45	20	7	8	31						
	σ^{s} D	12	52	22	7	7	8	fcc^{exp}	N/A	<6	N/A	N/A	N/A
	I	19	59	3	14	5		μ^{exp}	~20–21	~38–40	~19	N/A	N/A
	fcc^{s} D	20	18	26	16	20	92						
	I	18	14	2	37	29							
Co*V*FeMnNi		Co	*V*	Fe	Mn	Ni	V%		Co	*V*	Fe	Mn	Ni
	fcc^{eq}	20	20	20	20	20	100						
	fcc^{s} D	22	16	22	19	21	92	fcc^{exp}	N/A	N/A	N/A	N/A	N/A
	I	17	24	12	23	24		σ^{exp}	N/A	28	N/A	N/A	N/A
	bcc^{s} D	15	35	22	17	11	8						
	I	14	38	15	19	14							
CoCr*V*MnNi		Co	Cr	*V*	Mn	Ni	V%		Co	Cr	*V*	Mn	Ni
	fcc^{eq}	22	15	17	22	24	68						
	bcc^{eq}	15	30	26	17	12	32						
	bcc^{s} D	15	35	25	14	11	40	fcc^{exp}	N/A	N/A	N/A	N/A	N/A
	I	10	10	27	33	20		σ^{exp}	N/A	N/A	N/A	N/A	N/A
	fcc^{s} D	25	17	17	19	22	60						
	I	13	6	19	34	28							

simulation does not reliably predict the occurring phases, as found for the case of *Ti*CrFeMnNi. As for CoCr*V*MnNi, due to insufficient reported experimental data, *i.e.* the missing phase compositions, it is not clear which category it falls in.

As pointed out by Zhang et al. [36], in most cases, the observed single solid solution phase in HEAs is the "primary solidified phase". The "primary solidified phase" does not necessarily mean the phase directly below the solidus in the phase diagram, unless the equilibrium state is achieved, which, however, rarely happens in common

metallurgical operations. Thus, the "primary solidified phase" should be the phase in the non-equilibrium solidification process, which can be estimated, for example, by using the Scheil model.

One example for that is the system Co*V*FeMnNi as discussed in the preceding subsection. The equilibrium solid phase predicted to occur below the solidus line is a single fcc solid solution. Due to the morphology of the phase diagram, however, the solidified phases predicted by the Scheil conditions are fcc plus bcc after a non-equilibrium solidification process. The observed mixture of fcc + σ observed in experiments [12] could be a consequence of the alloy being in an intermediate position between the as-cast and the equilibrium states. Only those systems which are predicted to be single solid solution phases both at equilibrium and also after non-equilibrium solidification appear to end up as single solid solution phases after casting, *i.e.* as observed for the system CoCrFeMnNi at non-equiatomic and equiatomic composition.

It should also be emphasized that on the isopleths of a multi-component system the morphology features leading to phase separation during a non-equilibrium solidification might not be visible. This is due to the fact that the phase diagram of a multi-component system is a multi-dimensional object *i.e.* the characteristic features indicating phase separation might not be displayed on a two-dimensional section that are taken through a multiple component phase diagram.

7. Summary and conclusions

In this study, we experimentally and theoretically investigated the phase stability of non-equiatomic composition HEAs, *i.e.* $Fe_xMn_{62-x}Ni_{30}Co_6Cr_2$. Here, we summarize our study:

1. DSC measurements on the as-cast $Fe_xMn_{62-x}Ni_{30}Co_6Cr_2$ materials from room temperature (~300 K) to 1573 K exhibited no solid state phase transformation. EBSD measurements on the materials annealed at 1473 K for 2 h followed by water quenching revealed a single fcc solid solution phase.
2. The equilibrium phase diagram obtained for $Fe_xMn_{62-x}Ni_{30}Co_6Cr_2$ by using CALPHAD simulations shows a single γ(fcc) solid solution phase at high temperature (>900 K), a two-phase region (γ(fcc) + α(bcc)) at intermediate temperatures, and a three phase region (γ(fcc) + α(bcc) + σ) around room temperature (300 K). The transition temperature between the single phase region and the two-phase region increases with higher Fe content, indicating that the stability of the α(bcc) phase increases with higher Fe content. the α(bcc) phase is practically a Fe–Co binary solid solution with a large content of Fe, *i.e.* ~70–90 at.%. The σ phase mainly consists of Fe, Mn and Cr, and its volume fraction is only 3% at 300 K. The main elements in γ(fcc) are Fe, Mn, and Ni.
3. By using the Scheil model, which enables us to theoretically probe a non-equilibrium solidification process, the solidified phase turns out to be a non-equilibrium fcc solid solution. Fe segregates into the dendrite, while Mn and Ni segregate into the interdendritic regions. Co and Cr slightly segregate into the dendrite. At the composition of $Fe_{22}Mn_{40}Ni_{30}Co_6Cr_2$, Fe is almost depleted in the interdendritic regions, and for the other compositions, there is no depletion either in the dendritic region or the interdendritic region. The segregation profile is not in favor of the nucleation and growth of the low temperature phases, *i.e.* α(bcc) and σ, since in α(bcc) Mn, Ni, and Cr are depleted, while in σ, Ni and Co are depleted. No depletion of Mn, Ni, or Co was found either in dendritic or in interdendritic regions. To form the low temperature phases, hence massive diffusion would have been required. This means that the corresponding HEA is not an entropy stabilized solid solution but a kinetically frozen-in yet non-equilibrium material. This in turn implies that the identification of future multicomponent solid solution alloys might also target slow diffusing elemental mixtures rather than entropy maximized compositions alone.
4. The Gibbs free energy of γ(fcc) is always lower than that of α(bcc) between 0 and 1500 K at the fixed compositions of $Fe_xMn_{62-x}Ni_{30}Co_6Cr_2$, indicating that a martensitic transformation from γ(fcc) to α(bcc) is thermodynamically not favorable.

We also extended our theoretical studies to other HEAs with equiatomic composition, and compared our results with the reported experiments by Otto et al. [12].

1. The equilibrium phases at 1273 K of equiatomic compositional CoCrFeMnNi and Co*Mo*FeMnNi predicted by CALPHAD are in good agreement with the experimental observations by Otto et al. [12]. The experimentally observed phases of CoCrFeMn*Cu* and Co*V*FeMnNi are probably at the transient state between the as-cast state and the equilibrium state predicted by CALPHAD. By using CALPHAD, the non-equilibrium solidification process of *Ti*CrFeMnNi starts at ~1526 K and ends at ~678 K, which significantly deviates from the measured melting temperature, above 1237 K, implying the employed database in CALPHAD simulation is not reliable for the system *Ti*CrFeMnNi.
2. In addition to the proposed CALPHAD based HEA design approaches, *i.e.* the "matching element" approach by Zhang et al. [35] and the "high throughput" approach by Miracle et al. [38] and Senkov et al. [39], the effect of kinetic dominated metallurgical processes on the resulting constituent phases should be also taken into account. As exemplified by Co*V*FeMnNi at equiatomic composition, a phase separation occurs during the non-equilibrium solidification, though the equilibrium phase directly under the solidus line is a single fcc solid solution phase. Another important effect could be a possible martensitic transformation upon quenching.

Acknowledgments

D.M expresses his gratitude to Prof. Gerhard Inden for his lectures on ThermoCalc given at the Max-Planck Institut für Eisenforschung GmbH, Düsseldorf, Germany. Funding by the European Union is gratefully acknowledged, provided under the 7th Framework Programme (FP7/2007–2013) through the European Research Council (ERC) Advanced Grant SMARTMET agreement 290998.

References

[1] S. Ranganathan, Alloyed pleasures: multimetallic cocktails, Curr. Sci. 85 (10) (2003) 1404–1406. http://www.currentscience.ac.in/Downloads/article_id_085_10_1404_1406_0.pdf.
[2] J.W. Yeh, S.K. Chen, S.J. Lin, J.Y. Gan, T.S. Chin, T.T. Shun, et al., Nanostructured high-entropy alloys with multiple principal elements: novel alloy design concepts and outcomes, Adv. Eng. Mater. 6 (5) (2004) 299–303, http://dx.doi.org/10.1002/adem.200300567.
[3] J.W. Yeh, Alloy design strategies and future trends in high-entropy alloys, JOM 65 (12) (2013) 1759–1771, http://dx.doi.org/10.1007/s11837-013-0761-6. http://link.springer.com/10.1007/s11837-013-0761-6.
[4] Y. Zhang, T.T. Zuo, Z. Tang, M.C. Gao, K.A. Dahmen, P.K. Liaw, et al., Microstructures and properties of high-entropy alloys, Prog. Mater. Sci. 2014 61 (2013) 1–93, http://dx.doi.org/10.1016/j.pmatsci.2013.10.001. http://linkinghub.elsevier.com/retrieve/pii/S007964251300078.
[5] M.H. Tsai, J.W. Yeh, High-entropy alloys: a critical review, Mater. Res. Lett. 2 (3) (2014) 107–123, http://dx.doi.org/10.1080/21663831.2014.912690. http://www.tandfonline.com/doi/abs/10.1080/21663831.2014.912690.
[6] B. Cantor, Multicomponent and high entropy alloys, Entropy 16 (9) (2014) 4749–4768, http://dx.doi.org/10.3390/e16094749. http://www.mdpi.com/1099-4300/16/9/4749.
[7] A.J.B. Vincent, A study of three multicomponent alloys (BSc Part II thesis), University of Sussex, UK, 1981.

[8] P. Knight, Multicomponent alloys (BSc Part II thesis), University of Oxford, UK, 1995.
[9] B. Cantor, I. Chang, P. Knight, A. Vincent, Microstructural development in equiatomic multicomponent alloys, Mater. Sci. Eng. A 375–377 (2004) 213–218, http://dx.doi.org/10.1016/j.msea.2003.10.257. http://linkinghub.elsevier.com/retrieve/pii/S0921509303009936.
[10] B. Cantor, F. Audebert, M. Galano, K. Kim, I. Stone, P.J. Warren, Novel multicomponent alloys, J. Metastable Nanocryst. Mater. 24–25 (2005) 1–6, http://dx.doi.org/10.4028/www.scientific.net/JMNM.24-25.1. http://www.scientific.net/JMNM.24-25.1.
[11] S. Singh, N. Wanderka, K. Kiefer, K. Siemensmeyer, J. Banhart, Effect of decomposition of the Cr–Fe–Co rich phase of AlCoCrCuFeNi high entropy alloy on magnetic properties, Ultramicroscopy 111 (6) (2011) 619–622, http://dx.doi.org/10.1016/j.ultramic.2010.12.001. http://www.sciencedirect.com/science/article/pii/S0304399110003335.
[12] F. Otto, Y. Yang, H. Bei, E. George, Relative effects of enthalpy and entropy on the phase stability of equiatomic high-entropy alloys, Acta Mater. 61 (7) (2013) 2628–2638, http://dx.doi.org/10.1016/j.actamat.2013.01.042. http://linkinghub.elsevier.com/retrieve/pii/S1359645413000694.
[13] B. Gludovatz, A. Hohenwarter, D. Catoor, E.H. Chang, E.P. George, R.O. Ritchie, A fracture-resistant high-entropy alloy for cryogenic applications, Science 345 (6201) (2014) 1153–1158, http://dx.doi.org/10.1126/science.1254581. http://www.sciencemag.org/cgi/doi/10.1126/science.1254581.
[14] C. Zhu, Z. Lu, T. Nieh, Incipient plasticity and dislocation nucleation of FeCoCrNiMn high-entropy alloy, Acta Mater. 61 (8) (2013) 2993–3001, http://dx.doi.org/10.1016/j.actamat.2013.01.059. http://linkinghub.elsevier.com/retrieve/pii/S1359645413000980.
[15] J. He, C. Zhu, D. Zhou, W. Liu, T. Nieh, Z. Lu, Steady state flow of the FeCoNiCrMn high entropy alloy at elevated temperatures, Intermetallics 55 (2014) 9–14, http://dx.doi.org/10.1016/j.intermet.2014.06.015. http://linkinghub.elsevier.com/retrieve/pii/S0966979514001964.
[16] W. Woo, E.W. Huang, J.W. Yeh, H. Choo, C. Lee, S.Y. Tu, In-situ neutron diffraction studies on high-temperature deformation behavior in a CoCrFeMnNi high entropy alloy, Intermetallics 62 (0) (2015) 1–6, http://dx.doi.org/10.1016/j.intermet.2015.02.020. http://www.sciencedirect.com/science/article/pii/S0966979515000382.
[17] M. Yao, K. Pradeep, C. Tasan, D. Raabe, A novel, single phase, non-equiatomic FeMnNiCoCr high-entropy alloy with exceptional phase stability and tensile ductility, Scr. Mater. 72–73 (0) (2014) 5–8, http://dx.doi.org/10.1016/j.scriptamat.2013.09.030. http://www.sciencedirect.com/science/article/pii/S135964621300496X.
[18] C. Tasan, Y. Deng, K. Pradeep, M. Yao, H. Springer, D. Raabe, Composition dependence of phase stability, deformation mechanisms, and mechanical properties of the CoCrFeMnNi high-entropy alloy system, JOM 66 (10) (2014) 1993–2001, http://dx.doi.org/10.1007/s11837-014-1133-6.
[19] A. Miedema, P. de Châtel, F. de Boer, Cohesion in alloys – fundamentals of a semi-empirical model, Physica B+C 100 (1) (1980) 1–28, http://dx.doi.org/10.1016/0378-4363(80)90054-6. http://www.sciencedirect.com/science/article/pii/0378436380900546.
[20] B.Y. Zhang, Y.J. Zhou, J.P. Lin, G.L. Chen, P.K. Liaw, Solid-solution phase formation rules for multi-component alloys, Adv. Eng. Mater. 10 (6) (2008) 534–538, http://dx.doi.org/10.1002/adem.200700240.
[21] X. Yang, Y. Zhang, Prediction of high-entropy stabilized solid-solution in multi-component alloys, Mater. Chem. Phys. 132 (2–3) (2012) 233–238, http://dx.doi.org/10.1016/j.matchemphys.2011.11.021. http://linkinghub.elsevier.com/retrieve/pii/S0254058411009357.
[22] Y. Zhang, X. Yang, P.K. Liaw, Alloy design and properties optimization of high-entropy alloys, JOM 64 (7) (2012) 830–838, http://dx.doi.org/10.1007/s11837-012-0366-5. http://link.springer.com/10.1007/s11837-012-0366-5.
[23] M. Poletti, L. Battezzati, Electronic and thermodynamic criteria for the occurrence of high entropy alloys in metallic systems, Acta Mater. 75 (2014) 297–306, http://dx.doi.org/10.1016/j.actamat.2014.04.033. http://linkinghub.elsevier.com/retrieve/pii/S1359645414002845.
[24] S. Guo, C. Liu, Phase stability in high entropy alloys: Formation of solid-solution phase or amorphous phase, Prog. Nat. Sci.: Mater. Int. 21 (6) (2011) 433–446, http://dx.doi.org/10.1016/S1002-0071(12)60080-X. http://linkinghub.elsevier.com/retrieve/pii/S100200711260080X.
[25] S. Guo, C. Ng, J. Lu, C.T. Liu, Effect of valence electron concentration on stability of fcc or bcc phase in high entropy alloys, J. Appl. Phys. 109 (10) (2011) 103505, http://dx.doi.org/10.1063/1.3587228. http://scitation.aip.org/content/aip/journal/jap/109/10/10.1063/1.3587228.
[26] A.K. Singh, N. Kumar, A. Dwivedi, A. Subramaniam, A geometrical parameter for the formation of disordered solid solutions in multi-component alloys, Intermetallics 53 (0) (2014) 112–119, http://dx.doi.org/10.1016/j.intermet.2014.04.019. http://www.sciencedirect.com/science/article/pii/S0966979514001381.
[27] M. Widom, W. Huhn, S. Maiti, W. Steurer, Hybrid monte carlo/molecular dynamics simulation of a refractory metal high entropy alloy, Metall. Mater. Trans. A 45 (1) (2014) 196–200, http://dx.doi.org/10.1007/s11661-013-2000-8.
[28] W.P. Huhn, M. Widom, Prediction of A2 to B2 phase transition in the high-entropy alloy Mo–Nb–Ta–W, JOM 65 (12) (2013) 1772–1779, http://dx.doi.org/10.1007/s11837-013-0772-3.
[29] U. Kattner, The thermodynamic modeling of multicomponent phase equilibria, JOM 49 (12) (1997) 14–19, http://dx.doi.org/10.1007/s11837-997-0024-5.
[30] H. Springer, D. Raabe, Rapid alloy prototyping: compositional and thermo-mechanical high throughput bulk combinatorial design of structural materials based on the example of 30Mn–1.2C–*x*Al triplex steels, Acta Mater. 60 (12) (2012) 4950–4959, http://dx.doi.org/10.1016/j.actamat.2012.05.017. http://www.sciencedirect.com/science/article/pii/S1359645412003278.
[31] J.O. Andersson, T. Helander, L. Höglund, P. Shi, B. Sundman, Thermo-Calc & Dictra, computational tools for materials science, Calphad 26 (2) (2002) 273–312, http://dx.doi.org/10.1016/S0364-5916(02)00037-8. http://www.sciencedirect.com/science/article/pii/S0364591602000378.
[32] K.Y. Tsai, M.H. Tsai, J.W. Yeh, Sluggish diffusion in CoCrFeMnNi high-entropy alloys, Acta Mater. 61 (13) (2013) 4887–4897, http://dx.doi.org/10.1016/j.actamat.2013.04.058. http://linkinghub.elsevier.com/retrieve/pii/S1359645413003431.
[33] M.J. Yao, Non-equiatomic FeMnNiCoCr high entropy alloys: microstructure, phase stability and mechanical behavior (Master's thesis), Rheinisch-Westfälische Technische Hochschule Aachen, 2013.
[34] M. Laurent-Brocq, A. Akhatova, L. Perrière, S. Chebini, X. Sauvage, E. Leroy, et al., Insights into the phase diagram of the CrMnFeCoNi high entropy alloy, Acta Mater. 88 (2015) 355–365, http://dx.doi.org/10.1016/j.actamat.2015.01.068. http://www.sciencedirect.com/science/article/pii/S1359645415000816.
[35] F. Zhang, C. Zhang, S. Chen, J. Zhu, W. Cao, U. Kattner, An understanding of high entropy alloys from phase diagram calculations, Calphad 45 (2014) 1–10, http://dx.doi.org/10.1016/j.calphad.2013.10.006. http://linkinghub.elsevier.com/retrieve/pii/S0364591613001028.
[36] F. Zhang, C. Zhang, S. Chen, J. Zhu, W. Cao, U. Kattner, An understanding of high entropy alloys from phase diagram calculations, Calphad 45 (2014) 1–10, http://dx.doi.org/10.1016/j.calphad.2013.10.006. http://linkinghub.elsevier.com/retrieve/pii/S0364591613001028.
[37] K. Pradeep, N. Wanderka, P. Choi, J. Banhart, B. Murty, D. Raabe, Atomic-scale compositional characterization of a nanocrystalline AlCrCuFeNiZn high-entropy alloy using atom probe tomography, Acta Mater. 61 (12) (2013) 4696–4706, http://dx.doi.org/10.1016/j.actamat.2013.04.059. http://linkinghub.elsevier.com/retrieve/pii/S1359645413003443.
[38] D.B. Miracle, J.D. Miller, O.N. Senkov, C. Woodward, M.D. Uchic, J. Tiley, Exploration and development of high entropy alloys for structural applications, Entropy 16 (1) (2014) 494–525, http://dx.doi.org/10.3390/e16010494. http://www.mdpi.com/1099-4300/16/1/494.
[39] O.N. Senkov, J.D. Miller, D.B. Miracle, C. Woodward, Accelerated exploration of multi-principal element alloys with solid solution phases, Nat. Commun. 6 (2015) 1–10, http://dx.doi.org/10.1038/ncomms7529. http://www.nature.com/ncomms/2015/150305/ncomms7529/full/ncomms7529.html.